PAPER

Injected mass deposition thresholds for lithium granule instigated triggering of edge localized modes on EAST

IOP Publishing | International Atomic Energy Agency Nuclear Fusion

Nucl. Fusion **58** (2018) 036007 (11pp) https://doi.org/10.1088/1741-4326/aaa2ac

Injected mass deposition thresholds for lithium granule instigated triggering of edge localized modes on EAST

R. Lunsford[1,a], Z. Sun[2,a], R. Maingi[1], J.S. Hu[2], D. Mansfield[1], W. Xu[2], G.Z. Zuo[2], A. Diallo[1], T. Osborne[3], K. Tritz[4], J. Canik[5], M. Huang[2], X.C. Meng[6], X.Z. Gong[2], B.N. Wan[2], J.G. Li[2] and the EAST team[2]

[1] Princeton Plasma Physics Laboratory, Princeton, NJ 08543, United States of America
[2] Institute of Plasma Physics, Chinese Academy of Sciences, Hefei, Anhui 230031, People's Republic of China
[3] General Atomics, PO Box 85608, San Diego, CA 92186-5608, United States of America
[4] Johns Hopkins University, Baltimore, MD 21211, United States of America
[5] Oak Ridge National Laboratory, Oak Ridge, TN 37830, United States of America
[6] Department of Applied Physics, Hunan University, Changsha 410082, People's Republic of China

E-mail: rlunsfor@pppl.gov and sunzhen@ipp.ac.cn

Received 15 September 2017, revised 13 December 2017
Accepted for publication 19 December 2017
Published 16 January 2018

Abstract

The ability of an injected lithium granule to promptly trigger an edge localized mode (ELM) has been established in multiple experiments. By horizontally injecting granules ranging in diameter from 200 microns to 1 mm in diameter into the low field side of EAST H-mode discharges we have determined that granules with diameter >600 microns are successful in triggering ELMs more than 95% of the time. It was also demonstrated that below 600 microns the triggering efficiency decreased roughly with granule size. Granules were radially injected from the outer midplane with velocities ~80 m s^{-1} into EAST upper single null discharges with an ITER like tungsten monoblock divertor. These granules were individually tracked throughout their injection cycle in order to determine their efficacy at triggering an ELM. For those granules of sufficient size, ELM triggering was a prompt response to granule injection. By simulating the granule injection with an experimentally benchmarked neutral gas shielding (NGS) model, the ablatant mass deposition required to promptly trigger an ELM is calculated and the fractional mass deposition is determined.

Keywords: ELM triggering, lithium, EAST, Granule injection

(Some figures may appear in colour only in the online journal)

1. Introduction

The control of edge localized modes (ELMs) is critical for ITER. The particle and heat transfer from unmitigated ELMs to the plasma facing components (PFCs) shortens component lifetime resulting in a failure of the PFCs, and leading to extensive and costly recovery time. To avoid this circumstance, the rapid stimulated triggering of ELMs, termed 'ELM pacing' is explored. Of importance to the efficacy of this technique is the assurance that an injected pellet or granule will successfully trigger an ELM. When pacing with impurity granules, this concern needs to be balanced with the desire to minimize the impurity burden to the discharge to avoid substantial deleterious effects to the discharge performance.

The H-mode confinement phase of tokamak operation is enabled by the presence of a sheared perpendicular rotation profile which generates a particle and energy transport barrier [1]. The resulting pressure increase generates a density and

[a] The first two authors should be considered as equal co-authors.

temperature pedestal which often grows until becoming MHD unstable. These instabilities manifest as a periodic relaxation of the edge transport barrier, resulting in the spontaneous efflux of confined plasma [2] referred to as an ELM. As the H-mode barrier is otherwise highly effective at confining impurities, this flushing mechanism is helpful in reducing the core dilution due to impurity build-up. However, the ELM crash rapidly transports heat and particles to the PFCs. ELM effects on the PFCs are realized in two distinct manners. Cross field transport of filamentary structures has been observed [3] and these structures impact on the full toroidal extent of the internal vessel, leading to impurity sputtering and contamination of the discharge. Acceleration of ions through the electric sheath heats the PFCs on the order of 100 s of microseconds [4]. While allowing for the fact that the peak heat flux and power can indeed vary, the energy exhausted by an ELM, as normalized by the pedestal energy has been found [5] to be fairly uniform over a large operational space. In future burning plasma devices, where the ratio of plasma stored energy to surface area will be significantly larger than today's devices, the intensity of these outbursts becomes problematic as peak heat flux levels from unmitigated ELMs would significantly shorten divertor lifetimes [6].

To ameliorate these effects, various methods of ELM suppression and ELM mitigation are presently being explored. During ELM suppression, operation within an ELM free regime, such as those generated by lithium aerosol injection [7, 8], or operation in high transport regimes (e.g. caused by MHD activity such as edge coherent modes (ECM) [9] or I-mode operation [10]), removes the operative issues by eliminating the ELMs. During ELM mitigation, the mode activity is allowed but in such a way as to reduce its impact on the PFCs. Mitigation methods include [11]: impurity seeding [12], vertical jogs [13], rapid ELM triggering through supersonic molecular beam injection (SMBI) [14], and the two baseline ITER mitigation strategies of resonant magnetic perturbation (RMP) ELM pacing [15] and pellet ELM pacing [16]. In the technique described as 'pellet ELM pacing' mitigation occurs through a stimulated triggering of ELMs by the rapid injection of either small deuterium [17] or impurity pellets [18]. The mitigation realized in ELM pacing is dependent upon an assumed inverse relationship between the energy contained within an ELM and its triggering frequency [19] which reduces peak heat flux to the divertor. For this technique to be used as an operational tool, the triggering efficiency of the injected pellets or granules needs to approach unity for two reasons. First, a gap in the string of paced ELMs could result in the reassertion of a natural ELM cycle and the return of an unmitigated ELM, thus damaging the PFCs. Second, granule injections at a frequency greater than what is required for mitigation could lead to a sharp increase in overall Z_{eff}. While there are instances of improved plasma performance as a result elevated impurity concentration within the pedestal [12], an overaggressive injection size or frequency could dilute the main ion concentration within the burning plasma, thus decreasing the fusion power. To measure ELM triggering characteristics, lithium granules of multiple sizes were injected into EAST H-mode discharges to ascertain their likelihood of triggering an ELM.

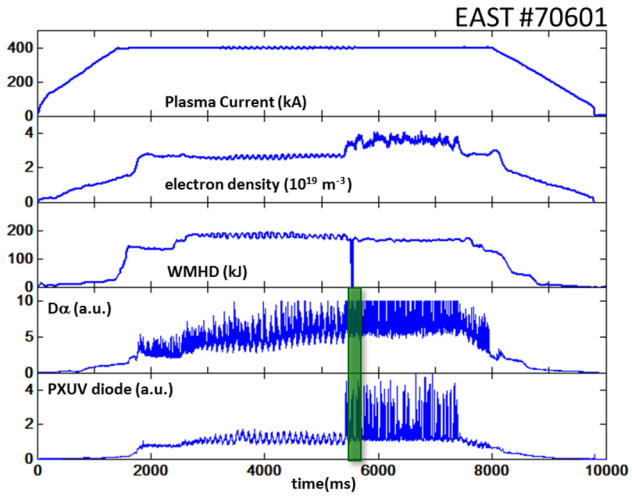

Figure 1. Typical discharge parameters for granule injection experiments. Time period for granule injection lasts from 5.5 to 7.5 s. The shaded bar in the lower two panels denotes the expanded time base featured in the top panel of figure 9.

Injection of lithium microgranules into the edge of EAST H-mode discharges has been shown [20] to produce pedestal localized pressure perturbations which can be sufficient to trigger an ELM. Present understanding [21] describes the creation of an ELM as an excursion of the pedestal pressure past a ballooning stability threshold. If the addition of an ablated microgranule drives the pedestal pressure into an unstable region of the parameter space the resulting localized plasma response is likely to result in the prompt triggering of an ELM. In the remainder of this paper we will describe the EAST experiments and the lithium granule injector (LGI), discuss the neutral gas shielding (NGS) model of granule ablation, and utilize this theory to model the granule ablatant deposition as it relates to the triggering efficiency of the injected granules.

2. EAST description

EAST is a fully superconducting tokamak device with RF dominant heating [22], primarily tasked with demonstrating high performance long pulse discharges in support of ITER and the conceptual China fusion engineering test reactor (CFETR) [23]. To support this mission, the EAST upper divertor was upgraded to an ITER-like Tungsten mono-block structure capable of exhausting 10 MW m^{-2}. Even with this upgraded PFC structure, heat flux management will be required for the targeted 1000 s long H-mode discharges. In addition, the active control of tungsten accumulation is a crucial issue to achieve long pulse operations. As such, EAST is equipped with a full complement of ELM triggering and control methods [24] such as RMP, SMBI, lower hybrid wave (LHW), lithium aerosol injection, impurity gas puffing, as well as deuterium pellet and lithium granule injection systems. Granule injection discharges, as shown in figure 1 were run with a nominal plasma

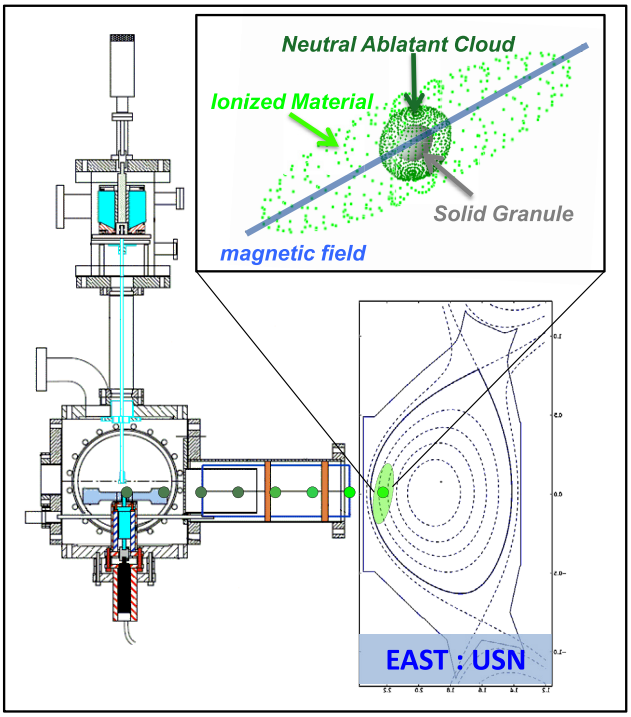

Figure 2. Cross section of the Granule Injector and diagram of granule injection. The inset image of the granule ablation displays the character of the granule and surrounding neutral and ionized clouds.

current of 400 kA, an average stored energy of 175 kJ, and auxiliary heating as follows: P(LHW1, 4.6 GHz) = 2 MW, P(LHW2, 2.45 GHz) = 0.3 MW, P(ECRH) = ~0.3 MW, P(NBI) = ~3.5 MW for a heating power total of 6.1 MW.

3. Injector description

The LGI installed at EAST is a modification of a piezoelectric aerosol injector first deployed on NSTX [25] and subsequently tested on EAST [26] is shown in figure 2. Since its inception, the powder injector has undergone a number of design improvements; principle among these is the ability to change granule size by active chamber selection without having to open the LGI to atmosphere. The granules drop from a 4-chamber reservoir in front of a turbine impeller which propels them horizontally into the low field side of the EAST discharge. For these experiments, granules were sorted into approximate sizes of 300, 500, 700, and 900 microns (±100 microns).

3.1. Granule tracking

In order to determine the ability of a single granule to trigger an ELM, it is necessary to track that particular granule from its exit from the drop tube all the way to full ablation within the discharge, and then correlate this with global plasma measurements to assess its success or failure in ELM triggering. In addition, as the granule injection frequency and the natural ELM frequency were often comparable, it is necessary to differentiate as much as is practicable, between spontaneous and

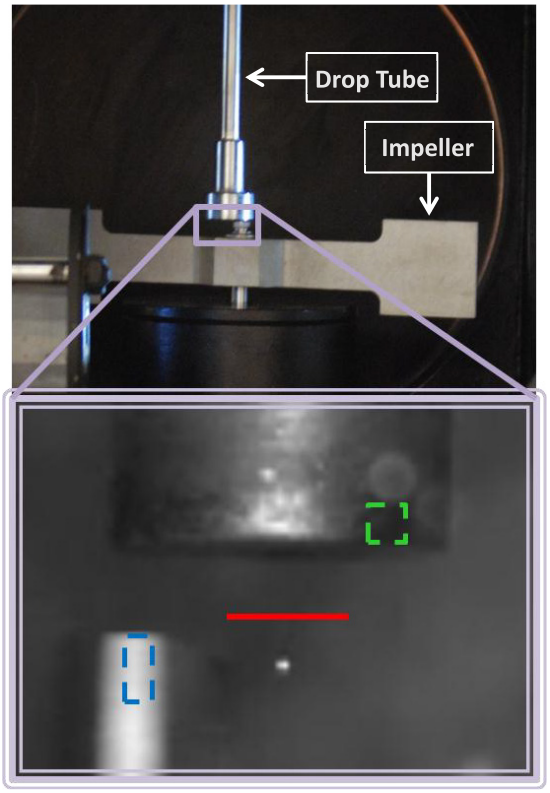

Figure 3. Enlarged image of the granule interaction region. The upper frame displays the drop tube and dual blade impeller, while the lower image is a magnification of the area within the upper box and shows a blade of the impeller (white vertical rectangle) about to strike a single lithium granule (white dot). Colored regions of interest are explained in the text and the frame is illuminated by external LED lighting.

stimulated ELMs. To accomplish this, the granule injection chamber and impeller are illuminated by external LED lights and observed on a high-speed framing camera. As is shown in figure 3 the image of the impeller is recorded and then subdivided into 3 sections of interest for analysis.

The rotation frequency of the impeller is determined by monitoring the illumination intensity within the blue square and from that an injection velocity for the granules is determined. The green box in the figure is located on a region of the guide tube known to illuminate with reflected light during granule ablation events. The illumination recorded in this area allows direct measurement of the elapsed time between the granule injection and the ablation event. This data is then correlated to the images recorded with the ablation camera to further link granule ablations with injections.

The red line located below the guide tube and immediately above the impeller path denotes the region chosen to monitor granule dropper events. The pixel intensities along this line are recorded for each camera frame and compiled in a single output file. As the velocity of a gravitationally accelerated granule immediately prior to contact with the impeller is such that the granule transits approximately one vertical pixel per frame, the stored lineout can be utilized as a data reduced record of the drop history. From this record both granule number and size can be determined, as is shown in figure 4. The two peaks visible in the above surface graph are records

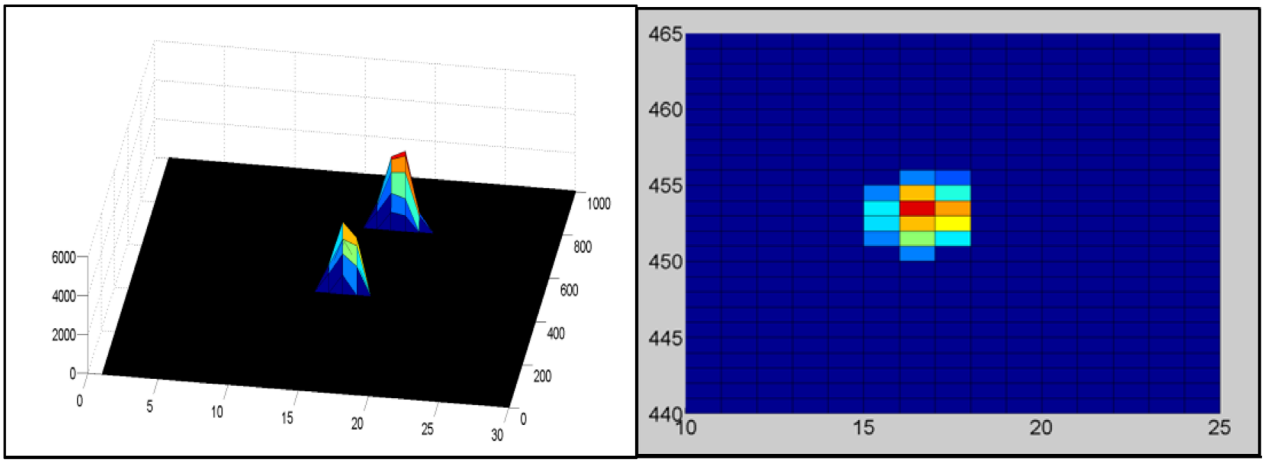

Figure 4. The two peaks visible in the above surface graph (left) are records of the falling granules which passed by the record line during the 1000 frames examined within this clip. Zooming in on one of the granule events (right) it is possible to resolve the extent of the granule both in spatial width along the x-axis as well as the duration of the granules passing the line of record as recorded on the y-axis. The color scheme is representative of the intensity recorded on the camera CCD.

of the falling granules which passed by the line during the 1000 frames examined within this clip. By expanding the axes of the plot around one of the granule events, it is possible to resolve the extent of the granule both in spatial width along the x-axis as well as the duration of the granules passing the line of record as recorded on the y-axis.

3.2. Determining granule size

To determine a granule mass dependence upon triggering efficiency the granules need to be individually sized *in situ* immediately prior to their injection. As the variation between granules sizes is on the order of the calibrated single pixel resolution of 135 microns, a sub-pixel analysis technique was adopted to augment the measurement and thus allow for a more accurate determination of the granule size threshold. Utilizing the assumption that the intensity of the reflection from a spherical granule (I_g) of diameter D_g is directly proportional to the illuminated area of the falling granule normal to the camera lens, the relationship between the two can be described by

$$I_g = \alpha * \pi \left(\frac{D_g}{2}\right)^2, \quad (1)$$

where α is a calibration constant which accounts for the collection efficiency of the optical train and should be identical for all granule sizes. To determine α, the full set of granules from EAST discharge #70601, known to have an average diameter of 900 microns by sieve sorting, were monitored to determine their reflected illumination. The average illumination from this measurement, along with an average diameter of 900 microns was used to determine the numerical value of α to be 0.044. This value was then utilized when determining the size of each individual granule across the full range (900, 700, 500 & 300 μm) to an accuracy of $\pm$0.5 pixels (~75 microns). We note that while this was very successful in determining sizes for the larger granules, the smallest granules are undersized by this methodology by 15% when compared to the overall size expected by previous sorting of the granules. We believe this to be due to the fact that these granule sizes are nearly the same as the single pixel resolution afforded by the camera.

3.3. Granule velocity and time of flight

Once the granule has been driven by the impeller into the flight tube it is lost from view. In order to ensure that the granule tracking remains consistent, the measurement of granule velocity and flight time is cross-correlated in three independent ways. The first method of determining granule velocity is by examining the rotation velocity of the impeller. While malleable lithium granules deform over the course of the impact with the impeller, the coefficient of restitution (C_R) is well known [27] at $C_R = 0.3$. Therefore, if the rotation velocity of the impeller is known an approximate velocity for the granules can be calculated by $v_g = (1 + C_R) * (2\pi r_i * f_i/2)$ where r_i and f_i are the impeller radius at the granule impact location and the rotation frequency of a single blade of the dual blade impeller. These are the velocities listed in column three of table 1. Additionally, images of granules recently impacted by the impeller and within free flight are examined. For a recently impacted granule, the spatial extent of the granule within the image is extended due to the granule's movement during the exposure, and thus the spatial extent of the image, divided by the exposure time is a direct measurement of the granule velocity. Free flight granule traces were examined for discharge 70605, in these the granule images were distributed over 25–30 pixels during the 48.7 μs exposure leading to granule velocities ranging from 70–83 m s^{-1} giving a rough velocity estimation error of $\pm$5 m s^{-1}.

As a final confirmation the granule injector was operated at an injection frequency of a few Hz. When the injection period is longer than the full flight time of the granule this allows each granule to be individually tracked from drop through full ablation prior to the next granule's introduction into the injection train. At these frequencies the one-to-one correlation

Table 1. Injection parameters for high power granule discharges.

Shot number	Average granule size (μm)	Average injection velocity (m s^{-1})	Number of injected granules	Average granule injection frequency (Hz)
70601	900	73 ± 5 m s^{-1}	151	70
70602	900	86	78	82
70603	810	82	409	111
70604	800	79	466	126
70605	610[a]	79	780	205
70606	460	78	911	309
70607	260	75	2175	551[b]

[a] Discharge #70605 was undertaken immediately after switching granule sizes without clearing the crystal surface. As such the average granule size at the beginning of the discharge is larger than the sizes at the end.
[b] For the smallest granule sizes injected in discharge #70607 the impeller was driving in multiple granules per pass, thus the actual frequency is capped by the 300 Hz impeller frequency. The uncertainty indicated in row 2 of column 3 is indicative of the uncertainty in all velocity estimates.

between the injection and ablation events and the known distance from injector to plasma edge provides a measurement of granule velocity. All three of these methods provided a consistent measurement of the granule flight time, allowing injected granules to be individually tagged and monitored throughout the experiment which then provides the ability to determine if an individual granule is successful in triggering an ELM. The overall injection characteristics for the lithium granule experiments performed at EAST and discussed in this paper are summarized in table 1.

4. Granule ablation and mass deposition

Previous experiments involving the injection of impurity pellets and granules into various devices [28] have found the ablation characteristics to be consistent with a NGS model which has been successfully applied for some time with Deuterium pellet injection [29]. In this model the injected and initially unshielded granule has its outer surface layer rapidly ablated by fast electrons as it enters the far scrape-off layer. This neutral ablatant cloud then shields the granule from further heating by absorbing additional energy influx. The shielding cloud mediates the interaction between the solid granule and the surrounding plasma; as the shielding cloud is ionized, the impurity ions stream away from the source granule creating a luminous oblate spheroid aligned with the local magnetic field as shown in the insert in figure 2. This relationship between the injected granule and neutral ablatant cloud is maintained until the pellet mass is exhausted. The typical granule ablation lifetime is displayed in figure 5 which shows multiple frames from a dedicated camera system which observes granule injection. The camera view is directed radially inward and filtered to view singly ionized lithium at 548 nm. The uppermost frame, enhanced to show additional details, is the first indication of a granule entering the discharge area, and begins to display elongated alignment concurrent with the 6° pitch of the local magnetic field. The second frame shows the formation of the dense neutral cloud which spherically surrounds the source granule. In the following frames this cloud becomes itself obscured by the field aligned ionization cloud which saturates the detector and continues to mask the source granule throughout the remainder of the frames. The extent of the field aligned ablation cloud can be shown in the true colour wide-angle camera view (figure 6: #70603 @ 4.498 s) observing the global discharge.

4.1. Benchmarking the NGS model with ablation histories

The ablation rate of the injected granule is proportional to the granule shielding factor η which is a measurement of the effectiveness of the intervening neutral cloud in its mitigation of the incoming heat flux. The NGS model, as described in [30–32] provides the physical underpinnings for the formation and evolution of the dense shielding cloud and sets the ablation rate of the injected granule (G) as governed by the equation:

$$G = \frac{8\pi}{25} q_s \eta \xi_g. \tag{2}$$

Where q_s is the convective heat flux to the granule as defined by:

$$q_s = \frac{1}{2} n_e T_e \left(\frac{8T_e}{\pi m_e} \right)^{1/2}. \tag{3}$$

With n_e, T_e and m_e as the electron density, temperature and mass respectively. While transiting the SOL there is the possibility of a contribution from a convective heat flux however the reduced temperatures and densities as well as the limited dwell time within this region of the plasma allow us to neglect this effect in these models. In addition as the granules are expected to fully ablate prior to approaching the magnetic axis and thus will not maintain residence on a single rational flux surface for an extended period of time the electron temperature and densities are assumed to maintain a pre-granule value. The granule physical parameters are subsumed within the variable ξ_g which contains the granule radius r_g, granule density n_g, the sublimation energy of a lithium granule ΔH (1.6 eV/atom) and the granule surface temperature T_s (taken here to be the boiling point of lithium at 0.14 eV) and is denoted by

$$\xi_g = \frac{r_g^2}{n_g} \left[\Delta H + \frac{10}{3} T_s \right]^{-1}. \tag{4}$$

By averaging a vertical cord of the Thomson scattering diagnostic at $R = 1.9$ m during discharge #70603 from 2.9 to 4.5 s (prior to granule injection) we are able to reconstruct the electron temperature and density profiles for the discharge as

Figure 5. Selected frames captured during injection of an ~700 micron lithium granule displays the stages of the ablation event. Frame 1 brightened to show detail.

shown in figure 7. By scaling the profiles by the ratio of the minor radius to the separatrix we can create a radial profile suitable for simulation of a low field side granule injection. In this model, the only parameter not known *a priori* is the granule shielding factor η, nominally a measure of the effectiveness of the granule at shielding the incoming flux. We therefore employ this as a fit parameter for the model. Since adjusting the granule shielding factor varies the temporal duration of an ablation event, we benchmark the NGS model by matching the calculated and observed pellet lifetimes. As the granule shielding factor for lithium granule injections into DIII-D was found to be approximately 0.3 ± 0.1 [33] this value was utilized for initial simulations of granule injection into EAST. With $\eta = 0.3$ we compare the digitized ablation traces from a representative set of granules to the calculated ablation rate determined by NGS simulation.

The ablation trace signal, as shown in figure 8, is the result of an integration of the intensity recorded on the dedicated ablation camera, images of which are shown in figure 5. The granule ablation signals were recorded during 4 separate discharges and compiled into a single record. Overlaid on this is the results of the NGS injection calculation for these granule sizes. The abrupt flattening of the ablation signal, most obvious in the 900 mm and 740 mm granule traces are the result of a saturation of the camera detector for these granule sizes, as can be seen in the 4th frame of figure 5. The relevant metric needed to benchmark these simulations was the ability to match the time envelope of the granule injection event to that of the NGS calculation. Utilizing the largest granule injection we can see that the calculated ablation duration of 1.2 ms is within 10% to the recorded granule ablation time of 1.3 ms. Therefore we adopt the DIII-D value for the granule shielding factor to simulate the ablation rate and granule penetration for 900, 740, 490 and 250 micron granules into the low field side of EAST discharges as shown in figure 9. As can be seen, the lithium granules quickly ablate upon entering the discharge. The smallest granules are consumed within the steep gradient region, whereas the larger granules penetrate up to 10 cm.

We note that for the smaller granules, the value chosen for the granule shielding factor predicts a pellet lifetime longer than experimentally observed. This indicates that the smaller granules are unable to fully support the neutral ablatant cloud assumed in this theory; hence, the model over-estimates the penetration depth of these granules.

4.2. ELM triggering physics

The mechanism whereby an injected impurity granule is responsible for the rapid triggering of an ELM is similar to that detailed for ELM triggering with Deuterium pellets as simulated by the non-linear MHD code JOREK [34]. When pellets or granules are injected into a plasma discharge they rapidly ablate leading to a localized density fluctuation. This density fluctuation is collisionally heated and ionized by field aligned free streaming electrons and the resultant pressure perturbation builds at a rate greater than the ion thermal diffusion. If this perturbative plasmoid is resident within the pedestal region, the induced pressure gradient increase coincident with the H-mode pedestal can drive ballooning type modes and trigger an ELM. Accompanied by a turbulent magnetic signature, the entrained plasma mass is ejected from the discharge and rapidly transmits the majority of the effusive energy onto the divertor PFCs [35].

5. Triggering efficiencies of injected granules

As described above we tag and track the granules throughout the injection process to determine their effectiveness at triggering ELMs. Granules are sized as they exit the drop tube prior to their impact with the impeller. Utilizing time of flight estimates outlined in section 3.3, and monitoring the area on

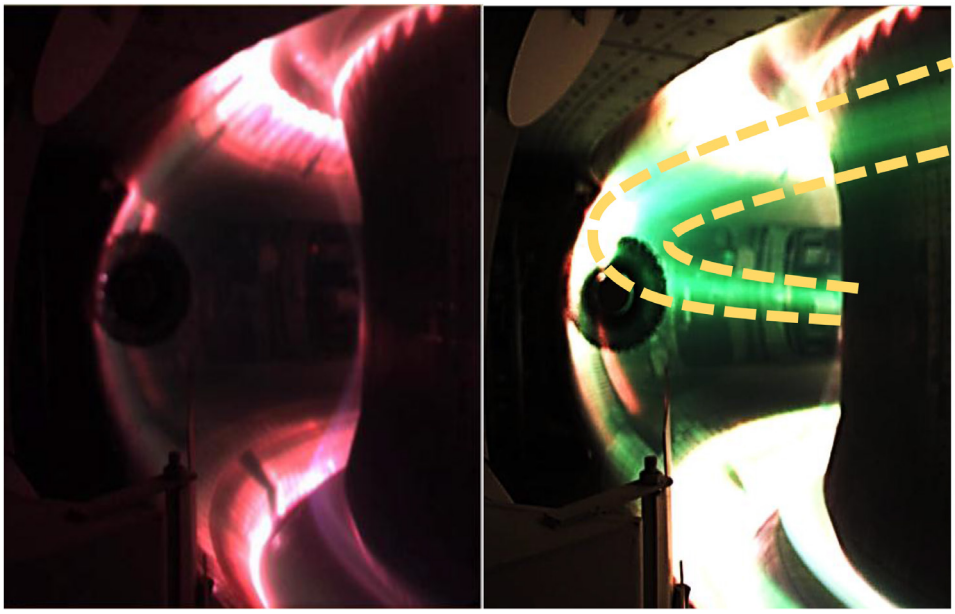

Figure 6. Wide angle true color camera view of EAST before(left) and during(right) a granule injection. While the core of the EAST torus obscures the granule injection location, the green field aligned lithium cloud resultant from the injection, and shown here bounded by the dotted lines, encircles the low field side of the discharge.

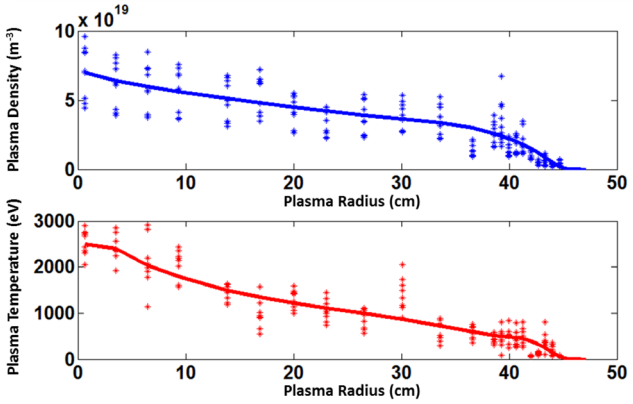

Figure 7. Averaged edge temperature and density profiles for EAST discharges used in granule injection simulation.

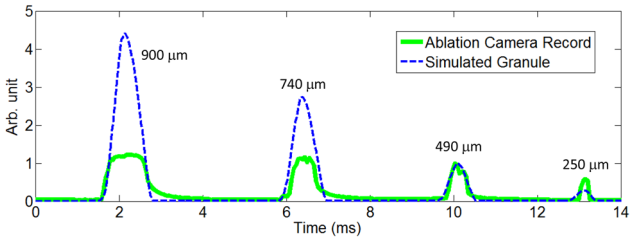

Figure 8. Ablation record and simulated granule ablation rates. The integrated ablation signals recorded during 4 separate granule injection discharges are compiled and compared to the ablation rates of simulated granules. The camera record and ablation rates are normalized to the peak of the 490 μm granule ablation. We note that saturation of the camera image, as shown in the 4th frame of figure 5, leads to a clipping of the peak height.

the dropper bobbin outlined by the green square as shown in the lower panel of figure 3 we are able to correlate the granule injection to an ablation event. The reflected ablation events observed by the impeller camera are then matched to events

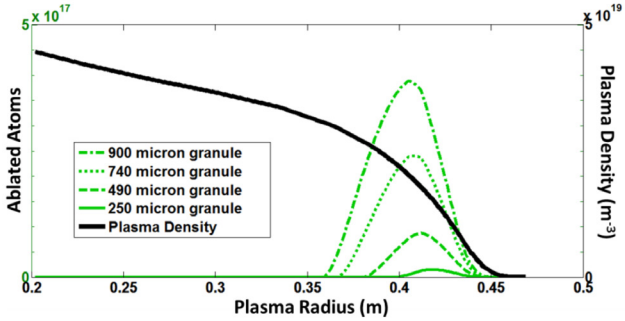

Figure 9. Granule Ablation simulations into EAST discharges. The edge density profile is overlaid to show granule penetration within the steep gradient region.

recoded on the ablation camera. This secondary camera directly records the discharge and allows observation of the stages and extent of the ablation event as shown in figure 5. Integrating the intensity recorded on these frames generates a time trace of the ablation events which is compared to spikes observed on the XUV diagnostic. Applying this methodology we were able to determine that each peak on the XUV diagnostic was indicative of the injection of a granule or, for the smallest size, a set of granules as described in section 5.2. To determine if the granule injection was successful in the triggering of an ELM we then compare the XUV and Dα diagnostic signals in the following manner.

First, a rolling background subtraction is run on both diagnostic signals to remove broad features and a peak detection algorithm is run on the XUV trace. This algorithm tags all likely injection events on the common time base. Using these tagged times, we examine a corresponding window in the Dα trace which starts at the time of the granule injection event and extends for 1 ms. If a Dα peak is located within this window, then the algorithm determines that the granule

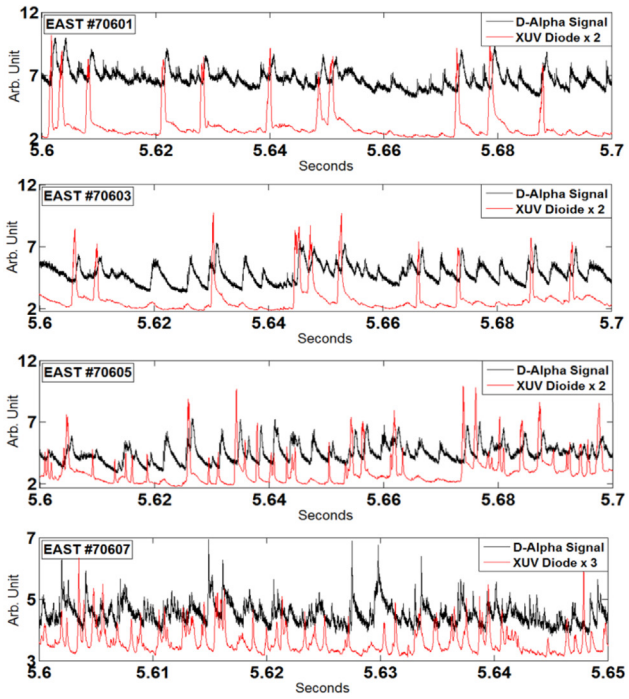

Figure 10. Dα and XUV traces for four representative granule injection time windows for similar EAST discharges. As is shown, for the top two graphs each peak within the lower trace corresponds to a peak in the upper trace showing triggering of an ELM, while the causal link is much less evident in the lower two traces.

injection was successful in promptly triggering an ELM. Examining the sequence of EAST granule injection discharges (70601–70607), a representative sample of which is shown in figure 10, the discharges are subdivided into 100 ms segments and then each subsection is tabulated to determine an average granule size and an overall triggering efficiency for the segment. For an ELMing H-mode discharge, such as those examined here, it is of course possible that the ELM event could be coincidentally and not causally related to the granule injection. These discharges roughly exhibited a natural 200 Hz ELM frequency, which means that each 100 ms segment could be expected to contain 20 ELMs, thus putting the probability that any 1 ms block might contain an ELM at 20%. If we approximate the granule injection frequency at 300 Hz, as was the case for ~500 micron granules, the probability that the XUV trace would contain a peak, thus indicating an injection event is approximately 30%. Thus, we can estimate that an overlap of these two probabilities would result in approximately 6% of natural ELMs being possibly mis-identified as triggered ELMs.

5.1. Granule size dependence and ELM energy losses

For granule diameters above 600 microns, there is near unity triggering efficiency for each of the time windows. However, below 600 microns the triggering efficiency decreased with granule size. We hypothesize that this is the result of an insufficient pressure perturbation being applied to the pedestal region. In figure 11 it can be seen that the triggering efficiency nominally varies between 40 and 95% for granule

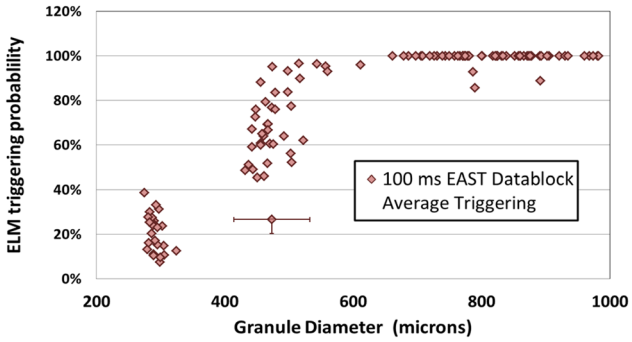

Figure 11. ELM triggering probability for assorted granule sizes. Each data point is representative of the average triggering probability observed during a subsection of an attempted ELM-pacing discharge. Error bars for the size estimate and triggering probability are shown for a representative granule. The vertical error bar characterizes the possibility that a natural ELM occurred coincident with a granule injection resulting in an overestimation of the triggering probability.

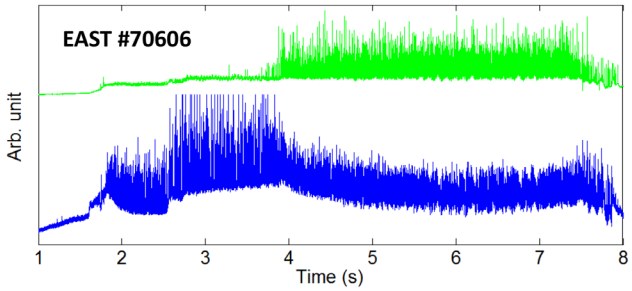

Figure 12. Comparison of ELM size before and during granule injection. Comparing the XUV diagnostic trace (upper, green) with the Dα signal (lower, blue) one observes a reduction of peak intensity by approximately a factor of 2 during the period of granule injection. This may indicate a reduction in ELM intensity.

diameters between 400 and 600 microns. Part of this variation is due to an interposition of large and small granules during a section of the discharges as discussed in the next section. Alternately, the wide variation in triggering efficiency can be explained by noting that when granule size is near the ELM triggering threshold, the time of injection relative the phase of the pedestal within the inter-ELM period sets the proximity of the unperturbed pedestal to the stability limit, thus resulting in different triggering efficiencies for similarly sized granules.

While not the primary focus of this research, it is illuminating to also briefly examine the ELM energy losses which result from repeated granule injection. There are several ways that ELM size can be assessed. As the ELM frequency is large, the energy contained within the individual elms is small, i.e. $\Delta W/W_{\mathrm{tot}} < 1$–2%, which is within the statistical uncertainty of the equilibrium reconstructions. So they are not resolvable with the data scale available. In addition the small size of the ELMs means that observations of the divertor hear flux through IR thermography is insufficient to resolve the small fluctuations. In an attempt to be able to quantify changes in the ELM size, we therefore examined the Dα trace as another, albeit imperfect, indicator of ELM size. This metric allows us to compare the relative intensities of the ELMs prior to

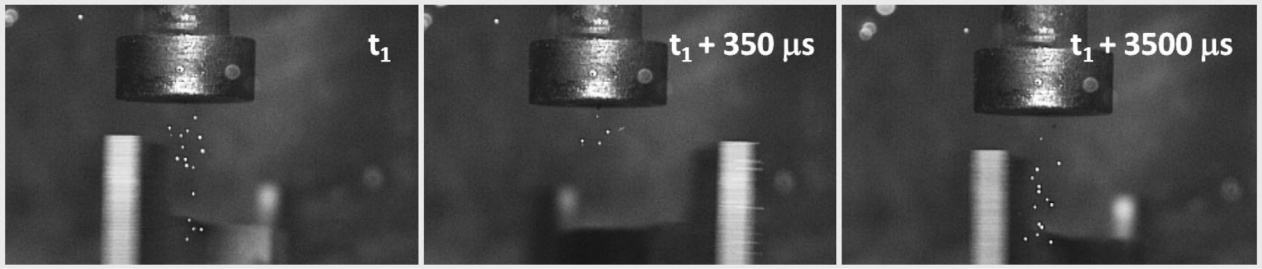

Figure 13. Filmstrip of two impeller passes and injection of 300 micron granules. Each pass of the impeller drives on the order of a dozen granules, seen here as single pixel white dots, into the discharge. The difference in plasma response between these sub-threshold granules and the larger variety will be explored in future work.

and during granule injection. We find that there is an effect on the Dα signal in response to granule injection thus possibly indicating a reduction in peak ELM intensity. For the larger granule sizes this is only about a 30% effect, consistent with the granule injection rate being smaller than the natural ELM frequency, and thus possibly augmenting but not substantially enhancing the ELM frequency. For the smaller sized granules, as the injection frequency is increased beyond the natural ELM frequency, we see a reduction of the overall Dα intensity by approximately factor of 2 as is shown in figure 12 for discharge 70606. Further study is required to better quantify this behavior and to ascertain in greater detail the effects of granule injection on overall discharge performance.

5.2. Sub-threshold granule perturbations

Here we discuss a facet of the injector operation that may affect the measured triggering efficiencies. The number of granules delivered from the dropper for a specific piezoelectric excitation voltage is inversely proportional to the size of the granules. Thus, while a certain voltage may result in well-separated granule injection for the larger sizes, a similar excitation will cause an overlapping cascade of the smaller granules. In figure 13, the granule throughput rate for the 300 micron granules is such that multiple granules are injected with each pass of the impeller. Accordingly, the injections result in a pulsed and distributed mass injection rather than the single overdense flux tube generated by the larger granules. Under these conditions the discrete granule injections may behave more like continuous powder injection.

We note this effect here simply to provide the caveat to the earlier analysis which suggests that there is an average triggering efficiency of 30% with these granules when in fact due to the multiple injections per impeller pass, the 'per granule' efficiency may be much lower than this, i.e. the displayed triggering efficiency graph should be treated as an upper bound.

5.3. Intra-shot granule variation

Granules are stored in four separate reservoirs above an injection chamber. The injection chamber sits overtop of the piezoelectric disk which is responsible for moving the granules to the drop tube. Over the normal course of operation, granules which are moved from the face of the piezoelectric disk for injection are replaced by a supply from the selected reservoir. At the termination of the active granule injection window the piezoelectric disk ceases vibration and the granules on the disk face remain in place. To ensure a uniformity of granule sizes the granule selection door is rotated halfway between openings, and the piezoelectric disk is activated to clear the disk face. Activation of the piezoelectric crystal for multiple seconds is required to insure that the disk face is clear of granules. Observation of the impeller camera during this time is used to confirm the cessation of granule drop events. If however, the granule selection door is fully rotated to a different reservoir, then the newly selected granules are deposited behind the inventory already on the piezoelectric disk. In this case the next activation of the piezoelectric disk would result in the introduction of a superposition of granule sizes, as the original size granules exit and are replaced by the newer size granules. This transition between granule sizes within a discharge was mapped in EAST (figure 14). During the initial granule injection phase of this discharge the nominal granule diameter for the 100 ms granule time blocks was approximately 800 microns, i.e. identical to the average granule size of discharges 70603 and 70604. After the first second of injection we note a sharp drop in granule diameter concurrent with a reduction in the granule triggering efficiency. Over the next 2 s of granule injection the average diameter of the granule dropped to just under 500 microns and the overall triggering efficiency was roughly 60%, consistent with the efficiency and size values observed during discharge #70605 of 65% and 460 microns respectively. Thus the point whereby the granule injection had a less than 90% chance of triggering an ELM can be seen to be below an approximate diameter of 600 microns. It is expected that this threshold will change with different discharge conditions and these are being compared with alternate granule injection discharges on EAST and with similar experiments on DIII-D.

5.4. Wall composition effects on ELM triggering

It is important to note that these experiments, while performed in upper-single null configuration on a W divertor, were obtained within an EAST vacuum vessel which still had a graphite lower divertor and thus a substantial carbon fraction coating the walls, in addition the PFCs were treated with lithium evaporative coatings of up to 30 g each morning prior to operations. In point of fact, the motility of adventitious carbon suggests that superposed over the tungsten surfaces is the presence of both a

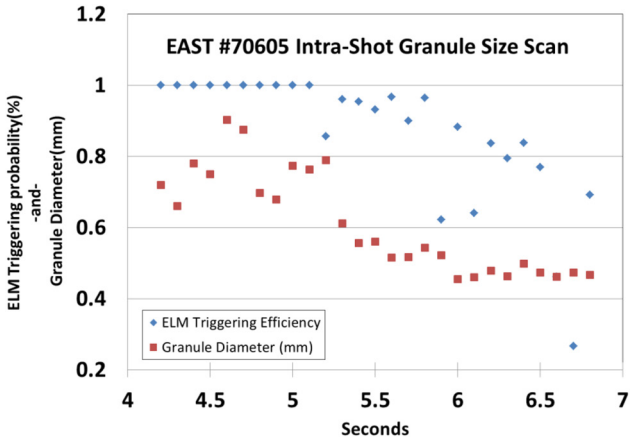

Figure 14. Intra-shot granule size scan. As a new reservoir is selected the average granule size over a 100 ms data block transitions from granule size 1 to granule size 2, as this switch crosses the triggering threshold a reduction in ELM triggering efficiency can be seen.

lithium and lithium carbonate coating. As such the changes in ELM triggering behaviour with the transition to all metal walls observed in both JET and AUG [36, 37], most specifically the presence of an ELM trigger lag time, which appears to be independent of instigating pellet size, cannot be directly compared to the experiments detailed here.

6. Summary and conclusion

The experiments on EAST utilized a range of sizes of injected granules which enabled the discernment of a granule mass threshold necessary for reliable ELM triggering. Using the duration of ablation to benchmark a NGS calculation we were able to determine the granule ablation rate and approximate location of mass deposition for various size granules. The largest granules penetrated approximately 13 cm into the discharge with a depositional barycentre at 7 cm, well inside of the plasma pedestal. By comparison the smallest granules had a peak mass deposition at 4 cm, i.e. just entering the steep gradient region.

As all granules injected in these experiments were travelling at roughly equivalent velocities, there is a correlation between granule size and penetration depth and thus ELM triggering efficiency. Consider that a single 600 micron granule contains approximately 5.24×10^{18} lithium atoms, a substantial fraction of which are deposited deep within the discharge, and is successful in providing prompt ELM triggering with an efficiency greater than 95%. In comparison, the injection of a dozen 300 micron granules (as shown in figure 13), most of which ablate at the pedestal foot, provide 7.86×10^{18} lithium atoms and is only able to generate an ELM event, on average 20% of the time. Thus we note that it is both the ability of the larger granules to survive the initial transit into the steep gradient region as well as the quantity of rapidly ablated remaining mass which is deposited deep within the plasma pedestal which enables these granules to generate conditions favourable to the creation of a ballooning instability.

While the conditions required for ELM triggering are well described, pressing issues involving the ELM pacing mitigation strategy remain, especially in all-metal PFC machines. In both ASDEX-Upgrade and JET deuterium pellet pacing experiments, the expected $1/f$ scaling of peak heat flux with increased pellet injection frequency was not observed. In addition, Li-granule ELM pacing in low torque DIII-D discharges displayed a bifurcated ELM structure whereby a mixed ELM regime with both large and small ELMs was observed [38]. Future experiments in EAST with planned upgrades to all-metal PFCs will facilitate a direct comparison to assess these issues in addition to determining the ELM triggering probability for higher heating power, higher plasma current, and lower collisionality plasmas in EAST.

Acknowledgments

This research was supported in part by the National Key Research and Development Program of China under Contract No. 2017YFA0402500 and the US Dept. of Energy Contracts DE-AC02-09CH11466, DE-FG02-09ER55012 and DE-FC02-04ER54698, and partly by the National Nature Science Foundation of China under Contract No. 11625524, No. 11605246, No. 11775261 We gratefully acknowledge the contributions from the EAST technical staff! The digital data for this paper can be found at http://arks.princeton.edu/ark:/88435/dsp01pk02cd394.

Notice: This manuscript is based upon work supported by the U.S. Department of Energy, Office of Science, Office of Fusion Energy Sciences, and has been authored by Princeton University under Contract Number DE-AC02-09CH11466 with the U.S. Department of Energy. The publisher, by accepting the article for publication acknowledges, that the United States Government retains a non-exclusive, paid-up, irrevocable, world-wide license to publish or reproduce the published form of this manuscript, or allow others to do so, for United States Government purposes.

References

[1] Wagner F. 2007 *Plasma Phys. Control. Fusion* **49** B1–33
[2] Leonard A.W. 2014 *Phys. Plasmas* **21** 090501
[3] Maqueda R.J. *et al* 2009 *J. Nucl. Mater.* **390–1** 843–6
[4] Loarte A. *et al* 2007 Progress in the ITER physics basis chapter 4: power and particle control *Nucl. Fusion* **47** S203
[5] Eich T. *et al* 2017 *Nucl. Mater. Energy* **12** 84–90
[6] Zhitlukhin A. *et al* 2007 *J. Nucl. Mater.* **363–5** 301–7
[7] Hu J.S. *et al* 2015 *Phys. Rev. Lett.* **114** 055001
[8] Maingi R. *et al* 2012 *Nucl. Fusion* **52** 083001
[9] Wang H.Q. 2014 *Phys. Rev. Lett.* **112** 185004
[10] Hubbard A.E. *et al* 2016 *Nucl. Fusion* **56** 086003
[11] Loarte A. *et al* 2014 *Nucl. Fusion* **54** 033007
[12] Frassinetti L. *et al* 2017 *Nucl. Fusion* **57** 022004
[13] Gerhardt S.P. *et al* 2010 *Nucl. Fusion* **50** 064015
[14] Hu J.S. *et al* 2015 *J. Nucl. Mater.* **463** 718–22
[15] Wade M.R. *et al* 2015 *Nucl. Fusion* **55** 023002
[16] Baylor L.R. 2016 *IEEE Trans. Plasma Sci.* **44** 1489
[17] Baylor L.R. *et al* 2015 *J. Nucl. Mater.* **463** 104–8

[18] Bortolon A. *et al* 2016 *Nucl. Fusion* **56** 056008
[19] Lang P.T. *et al* 2004 *Nucl. Fusion* **44** 665–7
[20] Sun Z. *et al* 2017 First results of ELM triggering with a multi-chamber lithium granule injector into EAST discharges *IEEE Trans. Plasma Sci.* PP 1–5
[21] Snyder P.B. 2004 *Plasma Phys. Control. Fusion* **46** A131–41
[22] Wan B.N. 2009 *Nucl. Fusion* **49** 104011
[23] Song Y.T. *et al* 2014 *IEEE Trans. Plasma Sci.* **42** 503
[24] Wan B.N. 2015 *Nucl. Fusion* **55** 104015
[25] Roquemore A.L. *et al* 2011 *Fusion Eng. Des.* **86** 1355
[26] Mansfield D.K. *et al* 2013 *Nucl. Fusion* **53** 113023
[27] Kuninaka H. and Hayakawa H. 2004 *Phys. Rev. Lett.* **93** 154301
[28] Lunsford R. *et al* 2017 *Nucl. Fusion* **57** 076008
[29] Pégourié B. 2007 *Plasma Phys. Control. Fusion* **49** R87
[30] Parks P.B. *et al* 1988 *Nucl. Fusion* **28** 477
[31] Parks P.B. *et al* 1994 *Nucl. Fusion* **34** 417
[32] Kocsis G. *et al* 1999 *Plasma Phys. Control. Fusion* **41** 881–98
[33] Lunsford R. *et al* 2016 *Fusion Eng. Des.* **112** 621
[34] Futatani S. *et al* 2014 *Nucl. Fusion* **54** 073008
[35] Huysmans G.T. *et al* 2009 *Plasma Phys. Control. Fusion* **51** 124012
[36] Lang P.T. *et al* 2013 *Nucl. Fusion* **53** 073010
[37] Lang P.T. *et al* 2014 *Nucl. Fusion* **54** 083009
[38] Bortolon A. *et al* 2017 *Nucl. Mater. Energy* **12** 1030–6